Tracking of Single Fluorescent Particles in Three Dimensions: Use of Cylindrical Optics to Encode Particle Position

H. Pin Kao and A. S. Verkman

Departments of Medicine and Physiology, Cardiovascular Research Institute and Bioengineering Graduate Group, University of California, San Francisco, California 94143-0521 USA

ABSTRACT We present a novel optical technique for three-dimensional tracking of single fluorescent particles using a modified epifluorescence microscope containing a weak cylindrical lens in the detection optics and a microstepper-controlled fine focus. Images of small, fluorescent particles were circular in focus but ellipsoidal above and below focus; the major axis of the ellipsoid shifted by 90° in going through focus. Particle z position was determined from the image shape and orientation by applying a peak detection algorithm to image projections along the x and y axes; x, y position was determined from the centroid of the particle image. Typical spatial resolution was 12 nm along the optical axis and 5 nm in the image plane with a maximum sampling rate of 3–4 Hz. The method was applied to track fluorescent particles in artificial solutions and living cells. In a solution of viscosity 30 cP, the mean squared distance (MSD) traveled by a 264 nm diameter rhodamine-labeled bead was linear with time to 20 s. The measured diffusion coefficient, 0.0558 ± 0.001 $\mu m^2/s$ (SE, $n = 4$), agreed with the theoretical value of 0.0556 $\mu m^2/s$. Statistical variability of MSD curves for a freely diffusing bead was in quantitative agreement with Monte Carlo simulations of three-dimensional random walks. In a porous glass matrix, the MSD data was curvilinear and showed reduced bead diffusion. In cytoplasm of Swiss 3T3 fibroblasts, bead diffusion was restricted. The water permeability in individual Chinese Hamster Ovary cells was measured from the z movement of a fluorescent bead fixed at the cell surface in response osmotic gradients; water permeability was increased by >threefold in cells expressing CHIP28 water channels. The simplicity and precision of this tracking method may be useful to quantify the complex trajectories of fluorescent particles in living cells.

INTRODUCTION

Single particle tracking (SPT) is a unique approach to monitor the directed and diffusive motions of individual particles in cellular compartments. Unlike fluorescence photobleaching recovery and autocorrelation spectroscopy, SPT provides information about the dynamics of single particle motion rather than ensemble-averaged information about populations of particles (Qian et al., 1991; Zhang et al., 1993). By analysis of particle trajectories, components of directed, diffusive, and restricted motion can in principle be resolved, and a direction can be assigned to the average motion of the particle (Sheetz et al., 1989).

Previous SPT studies have been limited to analysis of particle trajectory in two-dimensional systems. In general, a temporal series of images of small fluorescent or gold particles was analyzed to generate a series of x, y particle coordinates. Because only x and y were measured, SPT has been applied mainly for the analysis of the molecular mobility of proteins in 2D systems such as plasma membranes. Using gold-tagged concanavalin A in the plasma membrane of macrophages, Sheetz et al. (1989) reported that single receptors exhibited both random diffusive motion and directed motion at different times. Gross and Webb (1983) also observed random and directed mobility states for both individual molecules and clusters of fluorescently labeled LDL receptors on the surface of human fibroblasts. Two-dimensional SPT has also been applied to the analysis of kinesin movement in microtubules (Gelles et al., 1988), mitochondrial motion in liver cells (Salmeen et al., 1985), and cytoplasmic diffusion of gold particles (Geerts et al., 1987). The systems for these studies were either two-dimensional or two-dimensional projections of a three-dimensional system. A complete analysis of particle mobility in three-dimensional specimens requires determination of x, y, and z positions.

Several types of biological applications require three-dimensional SPT (3D SPT). By analogy to SPT studies of molecular diffusion in the plasma membrane, the three-dimensional motion of particles within the cytoplasm should be measurable. Intracellular traffic patterns could be monitored from the trajectories of labeled intracellular organelles or other subcellular components. Changes in cell shape and local cell membrane motion could be followed from the trajectories of immobilized particles at the cell surface.

We present a novel optical technique for 3D SPT of fluorescent particles in biological samples in real time. The technique is simple to implement, and its principle is applicable to other types of microscopy, including differential interference contrast microscopy. The three-dimensional position of a particle was encoded into its image by introducing a weak cylindrical lens into the optical detection path. Computer analysis of the shape, orientation, and position of the particle's image was applied to retrieve the x, y, and z coordinates. The 3D trajectory was then reconstructed from analysis of a temporal series of images. The spatial resolution and

Received for publication 25 February 1994 and in final form 8 June 1994.

Address reprint requests to Alan S. Verkman, M.D., Ph.D., 1246 Health Sciences East Tower, Cardiovascular Research Institute, University of California, San Francisco, CA 94143-0521. Tel.: 415-476-8530; Fax: 415-665-3847; E-mail: verkman@itsa.ucsf.edu.

0006-3495/94/09/1291/10 $2.00

optical requirements of the SPT instrument were evaluated, and applications in model and biological specimens are presented.

MATERIALS AND METHODS

Optical instrumentation

An epifluorescence microscope (Diaplan, Leitz, Rochleigh, NJ) was modified to carry out 3D SPT by incorporation of a cylindrical lens and microstepper motor; the computer algorithms to determine three-dimensional position are described in the Image Analysis section. Fluorescence was excited with a stabilized 100 W Hg-Xe arc lamp, 530 ± 20 interference filter, and 560 nm dichroic mirror, and detected through a 590 nm barrier filter. A long focal length cylindrical lens (focal length: 560 cm, J. L. Woods Optical Systems, Santa Ana, CA) was positioned in the detection path 15 mm beyond the exit aperture of the objective lens (Nikon CF Plan Apochromat 60 X/1.40 NA oil immersion). When viewed through this optical arrangement, a small particle appeared either ellipsoidal or circular depending upon its z position.

Images were collected by a charge-coupled device (CCD) camera (AT200 series; Photometrics Ltd., Tucson, AZ) with a TK512CB CCD chip (Tektronix Inc.; Beaverton, OR) contained within a camera housing cooled to −40°C (CH250; Photometrics). Images were digitized into a 512 × 512 pixel array at 14-bit resolution. Details of the optoelectronic characteristics of this camera were described previously (Zen et al., 1992). The axis of the cylindrical lens was aligned parallel to the rows of the CCD array. Pixel array size at the object plane with the 60 X objective lens and cylindrical lens was 261 × 263 nm.

The z position of the stage was controlled using a microstepper motor (Model CX indexer/drive unit with C57–51 motor, 12,800 steps/revolution; Compumotor Corp., Petaluma, CA) driving the fine focus control with a hard rubber coupling. The stage could be moved in 25 nm z increments. The vertical position of the microscope stage and image acquisition were controlled from a 25 MHz 486DX PC computer using software custom-written in Microsoft C 7.0. Software is available on request.

Analysis of particle position

The mean squared displacement (MSD) versus time relation was calculated for a particle trajectory as described by Qian et al. (1991). At times $t = n\Delta T$ ($n = 0, 1, 2, \cdots$) where ΔT is the sampling period, MSD $[\rho(t)]$ and MSD along each axis, $[\rho_x(t), \rho_y(t), \rho_z(t)]$, were calculated by

$$\rho_x(t) = \frac{1}{N}\sum_{i=1}^{N}(x_{i+n} - x_i)^2$$

$$\rho_y(t) = \frac{1}{N}\sum_{i=1}^{N}(y_{i+n} - y_i)^2 \qquad (1a)$$

$$\rho_z(t) = \frac{1}{N}\sum_{i=1}^{N}(z_{i+n} - z_i)^2$$

$$\rho(t) = \rho_x(t) + \rho_y(t) + \rho_z(t), \qquad (1b)$$

where N is the total number of positions recorded in the sequence. The diffusion coefficient, D, of the particle in three dimensions was calculated from the slope of the linear portion of a plot of $\rho(t)$ vs. t using the equation, $D = \rho(t)/6t$.

For some measured particle trajectories, there were discontinuities in the trajectory sequence because of required adjustments in the z position of the microscope stage (see Image Analysis). A continuous sequence was generated for analysis by Eq. 1, a and b by excluding these discontinuities from the sequence and adjusting the remaining positions and times of the sequence to account for the excluded point.

Preparation of artificial samples

Two types of samples were prepared based on the method of Hiraoka et al. (1990): samples containing immobilized fluorescent beads mounted within a liquid test specimen, and samples containing freely diffusing fluorescent beads. Red fluorescent latex beads (264 ± 9 [SD] nm diameter, excitation: 580 nm, emission: 605 nm) modified with surface sulfate groups (Molecular Probes, Eugene, OR) were used. To immobilize the beads at a depth of 0 μm into a liquid test specimen, beads were dried onto coverslips and 10 μl of glycerol was sandwiched between the coverslip and a larger glass slide so that the beads were in contact with the glycerol. The perimeter of the coverslip was sealed to the glass slide with clear nail enamel. To immobilize the beads at a specified depth, the procedure was reversed. Beads were dried onto a glass slide, and a microliter volume of the test solution (calculated from coverslip area and the desired solution layer thickness) was sandwiched between the slide and coverslip. Examination of samples by bright-field confocal microscopy confirmed sample thickness and bead immobility.

To prepare samples containing freely diffusing beads, microliter volumes of a bead suspension in water-glycerol solutions were sandwiched between a glass slide and coverslip to give a sample thickness of 30 μm. The sample was then sealed at the edges as above. To examine the effect of immobile barriers on bead diffusion, a fragment (≈5 × 5 mm) of porous glass filter (1.2 and 0.7 μm pore size, ≈250 μm thickness, Millipore Corp., Bedford, MA) was soaked in the bead-solution mixture for 1 min. The filter was placed between a coverslip and glass slide, excess bead-solution mixture was removed, and slight pressure was applied to the cover slip to eliminate air bubbles. Viscosities of the water-glycerol solutions were determined from the published reference tables (Miner and Dalton, 1953).

Cell culture

Swiss 3T3 fibroblasts (American Type Collection No. CL-101) were grown on 18 mm diameter round glass coverslips in DME-H21 supplemented with 5% fetal calf serum, 100 units/ml penicillin and 100 μg/ml streptomycin. Cells were maintained at 37°C in a 95% air/5% CO_2 incubator and used before confluence. Coverslips were transferred to a 200 μl-perfusion chamber (to facilitate rapid buffer changes) in which the cell-free surface of the coverglass was accessible to the objective. Chinese hamster ovary (CHO) cells were transfected with cDNA-encoding water channel CHIP28 using a mammalian expression vector with RSV promoter (Ma et al., 1993). Measurements were carried out 72 h after transfection.

Bead diffusion in cell cytoplasm

Red fluorescent latex beads (93 ± 7 [SD] nm diameter, excitation: 580 nm, emission: 605 nm) modified with surface carboxylate groups (Molecular Probes, Eugene, OR) were suspended in phosphate buffer saline (PBS) at 0.02 volume%. Microinjection pipettes were pulled from 0.9 mm ID borosilicate glass with omega dot fiber (FHC, Brunswick, ME) using a Kopf vertical pipette puller (David Kopf Instruments, Tujunga, CA). Approximately 5 fl of the suspension was microinjected into the cytoplasm of Swiss 3T3 fibroblasts using an Eppendorf microinjection apparatus (Microinjector 5242, Madison, WI).

Water permeability in individual cultured cells

To measure the water permeability of an individual cell, the z axis motion of 264 nm red fluorescent beads immobilized at the surface of CHO cells was measured in response to osmotic gradients. Cells were incubated with a PBS-bead solution (0.002 volume%) for 10 min at room temperature and then rinsed in PBS. The beads were immobilized on the cell surface at a density of ~1 bead/1000 μm^2. The z axis motion of a bead near the apex of the cell was measured in response to switching the perfusing medium rapidly between isosmolar (300 mOsm, PBS) and hypoosmolar (150 mOsm, 1:1 dilution of PBS with distilled water) buffers.

Computer simulations

To evaluate the statistical variation of the MSD plots measured for random diffusion, 3D random walks for a single particle were computed numerically by a modification of the method reported by Lee et al. (1991) for 2D diffusion. The random walks were generated on a cuboidal lattice whose spacing was arbitrarily selected as 10 nm. Trajectories started at the origin; at each particle position, one of six directions ($\pm x$, $\pm y$, $\pm z$) was selected randomly and particle position was moved to the adjacent lattice site in that direction. After every 100 such movements, the particle position was recorded. MSD plots for the simulated random walks with 100, 500, and 1500 recorded positions were computed by Eq. 1 for comparison with experimental data.

To simulate bead diffusion within cells (restricted diffusion), random walks were confined within a cube of specified size. At each particle position, the particle was moved to the randomly selected site only if that site was within the boundary of the cube; otherwise, the particle was not moved.

Image analysis

Encoding 3D position information into the image of a particle

To encode positional information into a particle's image, a weak cylindrical lens was introduced into the emission path of an epifluorescence microscope above the objective lens (Fig. 1, *left*). When a small, fluorescent particle was viewed through this microscope, either an ellipsoidal or a circular image was formed. The center of the image corresponded to the x and y positions of the particle. The orientation and shape of the image encoded the z position. If the particle's z position was in the focal plane, the image was smallest in size and circular in shape (Fig. 1, *right*). The images became larger and ellipsoidal away from the focal plane; the major axis of the ellipsoids formed above the focal plane was perpendicular to that formed below the focal plane. Images formed without the cylindrical lens were circular in shape (Fig. 1, *right*).

Algorithms for determination of x, y, and z positions

To determine particle position in three dimensions, binned projections of pixel intensity along the x and y axes of the image were analyzed. For a binned projection, each element, P_k, represents the sum of all pixels across the kth row or column of the image (Fig. 2 *A*):

$$P_k = \sum_{i=1}^{N} I_{i,k} \quad \text{or} \quad P_k = \sum_{j=1}^{N} I_{k,j}, \tag{2}$$

where $I_{i,j}$ is the pixel intensity at the position (i, j) and N is the total number of pixels along either the rows or columns of the array. Binned projections, rather than the collected 2D arrays, were processed because they contained sufficient information to determine a particle's position and required remarkably less computation time for position determination in real-time.

For the algorithms described below, an area-weighted quadratic fit was utilized to determine the contour of a binned projection over a single pixel length. Area-weighted fitting was used to construct a continuous contour because images were close to the pixel resolution of the camera (Inoué, 1986). As defined here, the coefficients, a_i, b_i, c_i, for the area-weighted fit, $\zeta_i(x) = a_i x^2 + b_i x + c_i$, over three adjacent bins, may be expressed in terms of the bin values, P_{i-1}, P_i, P_{i+1}. Three linear equations are obtained from the integral of $\zeta_i(x)$ over each bin: $\int_0^1 a_i x^2 + b_i x + c \, dx = P_{i-1}$, $\int_1^2 a_i x^2 + b_i x + c \, dx = P_i$, and $\int_2^3 a_i x^2 + b_i x + c \, dx = P_{i+1}$. The solution of these equations for a_i, b_i, and c_i is

$$\begin{bmatrix} a_i \\ b_i \\ c_i \end{bmatrix} = \frac{1}{6}\begin{bmatrix} 3 & -6 & 3 \\ -12 & 18 & -6 \\ 11 & -7 & 2 \end{bmatrix}\begin{bmatrix} P_{i-1} \\ P_i \\ P_{i+1} \end{bmatrix}, \tag{3}$$

where x is defined in units of pixel lengths, and $x = 0$ is at the left-most boundary of P_{i-1}. Because a_i, b_i, and c_i best define the contour over the central bin, Eq. 3 was used only over the length of the central bin, P_i.

For determination of x and y coordinates, the position of the maximum in the contour of each projection was determined. At the bin with the highest summed intensity, an area-weighted quadratic fit (Eq. 3) was applied. The position at the maximum of the quadratic fit, $-b_i/2a_i$, was taken as the position of the bead along that axis. The position of this maximum was insensitive to image intensity and offset.

For determination of z position, two algorithms were applied to detect the spread in the distribution of each projection. The first algorithm was designed to detect projection differences for large ellipsoidal images generated far from the focal plane. The second algorithm was designed to detect differences for smaller ellipsoids generated near the focal plane.

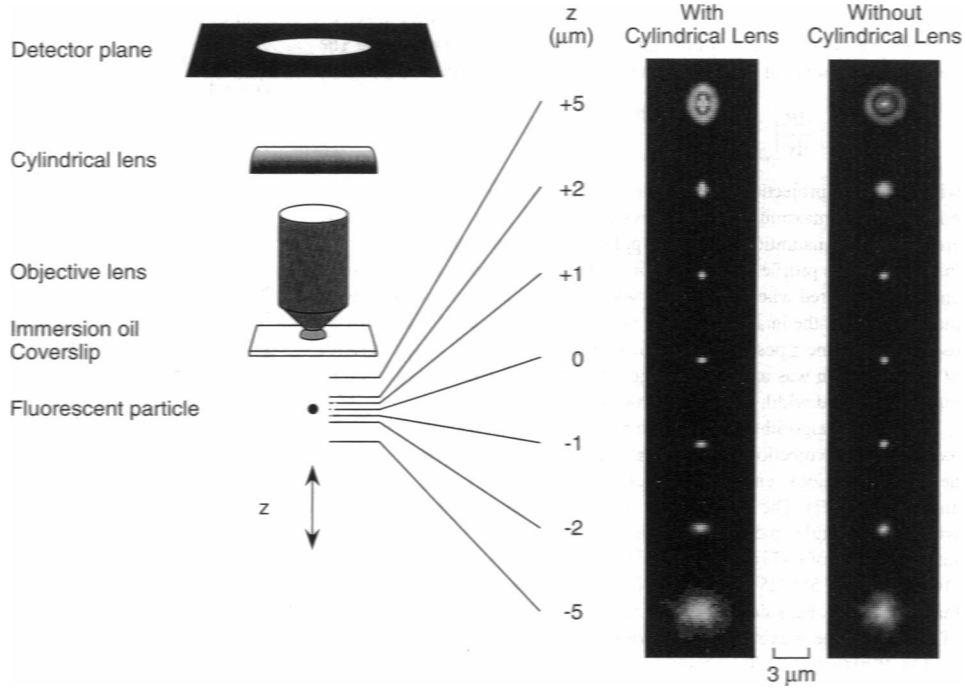

FIGURE 1 Asymmetry in images of a 264 nm red fluorescent latex bead produced by a cylindrical lens. The epifluorescence microscope was modified with a cylindrical lens and a microstepper motor for adjusting the z position of the stage (see text for details). Beads were imaged with a Nikon 60X oil immersion objective lens with n = 1.48 immersion oil. Indicated z positions are relative to the focal plane. Images are shown in the presence (*left*) and absence (*right*) of the cylindrical lens in the microscope emission path.

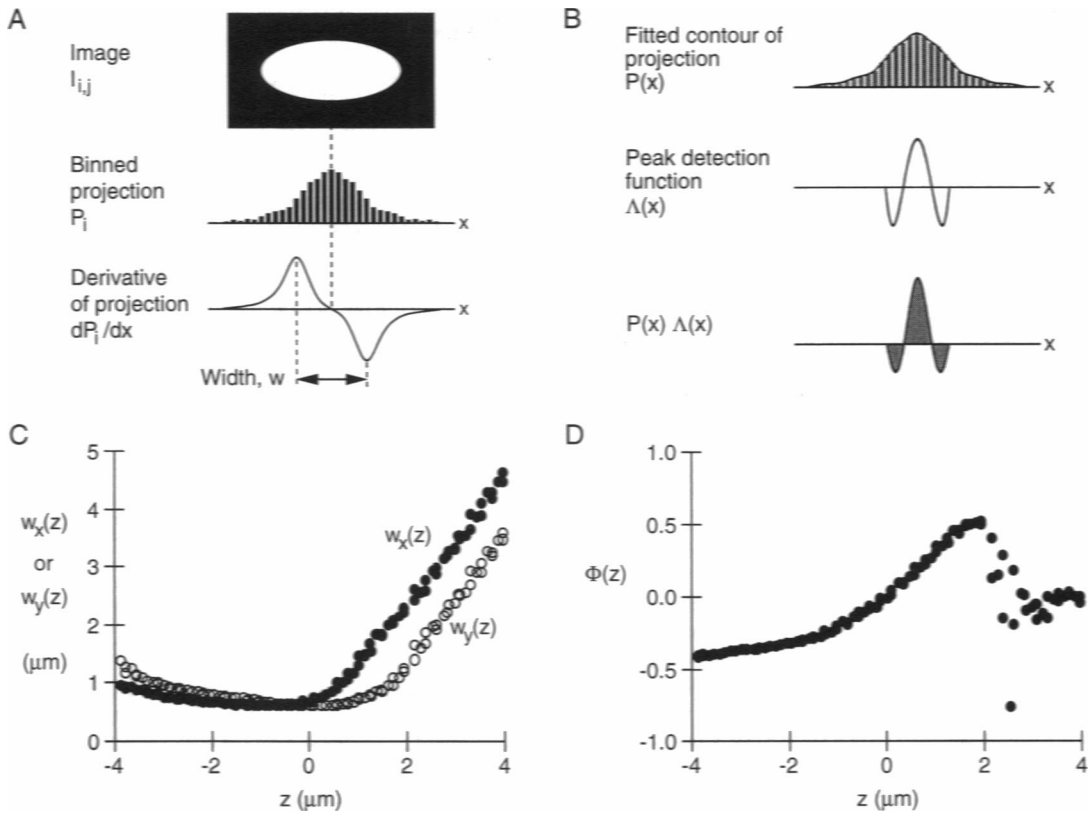

FIGURE 2 Determination of z position from image asymmetry. (*A*) Image width algorithm: the width, w, of the image along one axis was determined as the distance between the minimum and maximum of the derivative of the projection. (*B*) Peak detection algorithm: the fitted contour of the binned projection, $P(x)$, was multiplied by a peak detection function, $\Lambda(x)$. The area of the product, $\phi = \int P(x)\Lambda(x)\,dx$, as indicated by the shaded region, was used to calculate $\Phi(z)$ as defined in Eq. 6. (*C* and *D*) Representative calibration curves for $w_x(z)$, $w_y(z)$, and $\Phi(z)$ for a fixed 264 nm red fluorescent bead. Each point represents the average of five images taken of the bead at that position; SDs are smaller than the circle size. Images were collected as in Fig. 1.

The first algorithm for z position utilized the width of a binned projection along each axis (Fig. 2 *A*). The width, w, was calculated as the distance between the maximum and minimum derivatives of the P_i projection. The numerical derivative of the projection was calculated as (James et al., 1985)

$$\left.\frac{dP}{dx}\right|_{x=i} \approx \frac{P_{i-2} - 8P_{i-1} + 8P_{i+1} - P_{i+2}}{12}, \tag{4}$$

where x is the projection position, in pixel lengths. The positions of the minimum and maximum in the derivative profile were determined from area-weighted quadratic fits (Eq. 3) applied at the minimum and maximum in the derivative profile. The widths of the projection along each axis, $w_x(z)$ and $w_y(z)$, differed when the particle was not at the focal plane because of the ellipticity of the image. $w_x(z)$, $w_y(z)$, and their relative magnitudes were used to determine z position (see below). Because only the first derivative of the projection was analyzed, image intensity and offset had little effect on the measured width of the projections.

The second algorithm for z position applied one-dimensional peak detection to the projection for each axis. This algorithm is based on edge detection functions employed in digital image processing (Gonzalez and Wintz, 1987). The peak detection function must be convex in shape, with only a single maximum flanked by two minima, and have a total integrated area of 0 (Fig. 2 *B*). The single peak detection function, $\Lambda(x) = (16 - x^2)(16 - 5x^2)/256$, where x is in pixel lengths, was chosen to satisfy these properties. Peak detection was implemented by aligning the maximum of $\Lambda(x)$ with the maximum of the continuous contour of the binned projection, $P(x)$ (Fig. 2 *B*). The product of the two functions was then integrated from pixels -4 to $+4$. $P(x)$ was not determined as a continuous function, but as a set of fitted quadratic polynomials for each pixel, $\zeta_i(x)$, whose coefficients are defined by Eq. 3. The integral was evaluated as a discrete sum of integrals,

$$\begin{aligned}\phi &= \int_{-4}^{+4} \Lambda(x)P(x)\,dx \approx \sum_{i=-4}^{3} \int_{x=i}^{x=i+1} \Lambda(x)\zeta_i(x)\,dx \\ &= \sum_{i=-4}^{3} \int_{x=i}^{x=i+1} \left[\frac{1}{256}(16 - x^2)(16 - 5x^2)\right] \\ &\qquad \times [a_i(x - i + 1)^2 + b_i(x - i + 1) + c_i]\,dx,\end{aligned} \tag{5}$$

where x is the projection position in pixel lengths and $x = 0$ is defined as the center of the projection. The parameter ϕ is a measure of the spread of the projection distribution near the center of the projection. ϕ was maximum when the spread of the projection was small and decreased as the spread increased. The value of ϕ for the x and y projections, ϕ_x and ϕ_y, differed when the particle was not in the focal plane because of the elliptical shape of the image, as quantified by the function $\Phi(z)$,

$$\Phi(z) = \frac{\phi_y(z) - \phi_x(z)}{\phi_y(z) + \phi_x(z)}. \tag{6}$$

Measurement of z position utilizing calibration data

Calibration curves [$w_x(z)$, $w_y(z)$, and $\Phi(z)$] measured before an experiment were used to determine z position. Calibration data were collected using a

single immobilized reference bead with the same diameter as that used for subsequent SPT measurements. At 50 z positions from 5.75 μm below to 5.75 μm above the focal plane, five images of the single bead in each z plane were acquired. The average values and SDs for $w_x(z)$, $w_y(z)$, and $\Phi(z)$ of the five images were calculated. Calibration data consisted of three- to five sets of measurements, each for 50 z positions. To change the z position of the bead during collection of calibration data, the microscope stage was raised in steps of 0.23 μm; only upward steps were used to minimize errors from mechanical hysteresis of the fine focus control. Because of this hysteresis, the exact z position of the focal plane was determined by $\Phi(z)$ rather than from the absolute angular position of the motor shaft (see Discussion). All z positions for the calibration were reported relative to the focal plane ($z = 0$).

Representative calibration data for $w_x(z)$, $w_y(z)$, and $\Phi(z)$ are shown in Fig. 2, *C* and *D*. Both $w_x(z)$ and $w_y(z)$ reach minima; however, the minima were located at different positions on the z axis because the cylindrical lens magnifies along one axis only. $\Phi(z)$ monotonically increased as z position increased from -3 to $+2$ μm. $\Phi(z)$ did not increase beyond $+2$ μm because of the appearance of rings in the image (Fig. 1, *right*). The z focal plane position was determined based on the image symmetry ($\Phi(z) = 0$) at the focal plane. For each set of 50 z positions measured, $\Phi(z)$ was solved using a fifth order polynomial fitted to the five calibration data points centered at the focal plane.

During an experiment, z position was determined in real time from the values of $w_x(z)$, $w_y(z)$, and $\Phi(z)$ for a single image using the calibration curves. z position was first estimated as the average of the $w_x(z)$ and $w_y(z)$ estimates. If the bead was between -2 and 1.8 μm of the focal plane, a more accurate determination of z position was provided by $\Phi(z)$. If the bead was outside of the $z = -2$ to 1.8 μm region, the microstepper motor was used to position the bead to within 1 μm of the focal plane. The time required to reposition the bead was <0.5 s; particle tracking was not continued until 1 s after motor movement to reduce transient mechanical phenomena (such as shifting of the immersion oil).

Procedure for continuous 3D particle tracking

The 3D trajectory of a particle was determined in real time by applying the algorithms described above to a sequence of images. Before an experiment, calibration curves were measured. At the beginning of an experiment, a small rectangle (≈30 × 30 pixels) of the CCD array was selected that contained the particle to be tracked. An image was collected at an exposure time of 50 ms and analyzed to determine x, y, z position. The z position of the microscope stage was adjusted if the particle's z position was outside of the -2 and 1.8 μm range. The location of the rectangle on the CCD array was adjusted if particle's x or y positions were within 7 pixels of the boundary of the image. For analysis of particle trajectory, z positions were determined using $\Phi(z)$ (from -2 to 1.8 μm).

RESULTS

Precision and errors in 3D position measurement

Position measurements on immobilized beads were carried out to evaluate instrument precision. Factors that influence measurement precision include microscope vibration, mechanical stage drift, and detector signal and noise amplitudes. To estimate the SDs for position determination, σ_x, σ_y, and σ_z, the position of an immobilized bead located at z positions within 2 μm of the focal plane was measured. For random noise, $\rho^2(\Delta t)$ for an immobilized bead should be time-independent and equal to $2(\sigma_x^2 + \sigma_y^2 + \sigma_z^2)$ for $\Delta t > 0$; $\rho_x^2(\Delta t)$, $\rho_y^2(\Delta t)$, and $\rho_z^2(\Delta t)$ are also time-independent and equal to $2\sigma_x^2$, $2\sigma_y^2$, and $2\sigma_z^2$, respectively (Couch, 1987). The measured MSD plots shown in Fig. 3 *A* for a single z position are time-independent as predicted. The measurement errors for each axis as a function of z position are shown in Fig. 3 *B*. Errors along x and y showed little change in going from -2 to 1.8 μm around focus. Errors along z were greatest at -2 and 1.8 μm from focus because of the decreased image intensity and the low slope of $\Phi(z)$ at these positions. Minimum z error occurred at $z \approx 1$ μm above focus where spatial resolution, image intensity, and the slope of $\Phi(z)$ are optimum. Typical measurement SD (precision) was 5 nm along x, 2–3 nm along y, and 12 nm along z. It should be noted that these errors are much smaller than the scatter observed in $w_x(z)$, $w_y(z)$, and $\Phi(z)$ (Fig. 2, *C* and *D*). This scatter represents not the precision of the technique, but the composite effects of mechanical hysteresis and gear lash on the accuracy which limited the accuracy of z position determination. Because of this variability, many calibration data points were measured to construct the calibration curves.

The refractive index of the medium between the particle and objective lens affects the image formation properties of the microscope system (Gibson and Lanni, 1991). As a particle moves in the z direction within a sample, its calibration curves [$w_x(z)$, $w_y(z)$, and $\Phi(z)$] may change and introduce uncertainty in z position determination. To evaluate the effects of refractive index and sample thickness in our system, $w_x(z)$, $w_y(z)$, and $\Phi(z)$ were measured for beads immobilized at 0 and 20 μm depths in water ($n = 1.33$) and 83% aqueous-glycerol ($n = 1.45$) solution. The lens immersion fluid had a refractive index of 1.48. For the water sample, the shape of $\Phi(z)$ changed significantly for bead depths of 0 and 20 μm (Fig. 3 *C*). However, in the glycerol solution, the shape of $\Phi(z)$ showed little change (Fig. 3 *D*), suggesting that changes in the calibration curves with z position are small if the refractive indices of the sample and immersion oil are similar. The same conclusion was obtained from analysis of the $w_x(z)$ and $w_y(z)$ curves (not shown). For the diffusion measurements reported below, the instrument was calibrated using an immersion oil having a refractive index of 1.48, which was close to that of the sample media (1.44–1.45).

SPT of small beads in artificial systems

Fig. 4 *A* shows two representative trajectories of a small fluorescent latex bead in an aqueous solution containing 83% glycerol. The trajectories appeared to be random along all three axes. To determine whether these trajectories corresponded to random diffusive motion, MSD plots along the x, y, and z axes were constructed from a series of 1800 positions recorded every 0.54 s (Fig. 4 *B*). The plots were linear and overlapped over the first 5 s, suggesting that the particle diffused randomly in three dimensions. The divergence of the MSD plots beyond 5 s was caused by statistical variability of random walks.

$\rho(t)$ (in three dimensions) corresponding to the data provided in Fig. 4 *B* was linear from 0–20 s (Fig. 4 *C*). From the slope (see Materials and Methods), the diffusion coefficients for beads in water-glycerol solutions of viscosities 30 and 56 cP were 0.0558 ± 0.001 (SE, $n = 4$) and 0.0232 ± 0.001 (SE, $n = 4$) μm^2/s, respectively. For the conditions of

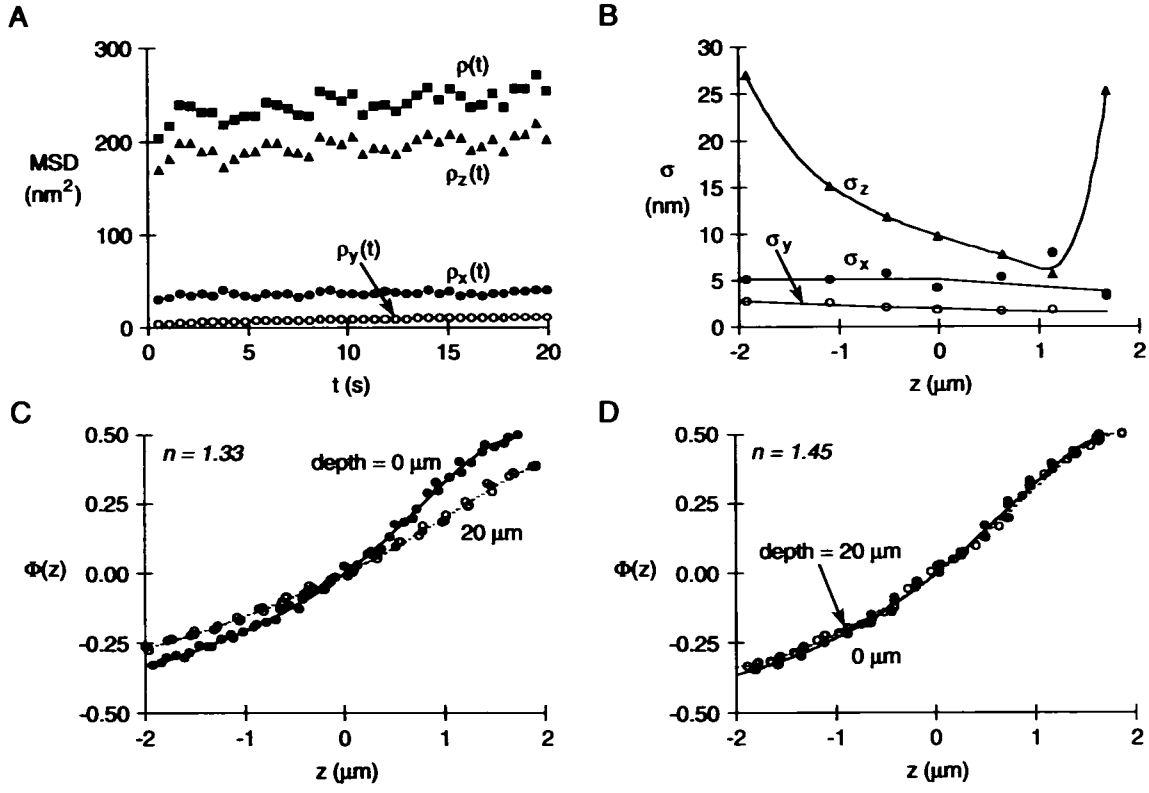

FIGURE 3 Measurement accuracy in 3D SPT. (*A*) Representative MSD curves for an immobilized 264 nm fluorescent bead located in the focal plane. (*B*) σ_x, σ_y, and σ_z as a function of z. Each point was determined from a trajectory ~600 steps sampled at a rate of ~2 Hz. (*C* and *D*) Dependence of $\Phi(z)$ for a bead immobilized at 0 μm and 20 μm into water (n = 1.33) (*C*) and 83% glycerol in water (n = 1.44) (*D*). Images were collected as in Fig. 1.

our experiments (27.5°C, particle radius = 264 nm), the Stokes-Einstein equation predicts diffusion coefficients of 0.0556 and 0.0295 $\mu m^2/s$, respectively, in agreement with the measured values.

Similar 3D SPT studies were carried out for bead diffusion in porous glass filters (1.2 and 0.7 μm pore sizes) soaked in a water-glycerol solution of viscosity 56 cP (Fig. 4 *D*). $\rho(t)$ decreased from its value in free solution as pore size decreased. The shape of $\rho(t)$ for particle diffusion in the filters demonstrated two regions: an increasing nearly linear region from 0 to ~5 s, and a linear region with decreased slope at >5 s. These regions probably correspond to short- and long range bead diffusion in the restricted environment. Qualitatively similar results were computed by Saxton (1989) for Monte Carlo simulations of mobile point particles diffusing in a two-dimensional lattice containing immobile obstacles, and by Pusey et al. (1979) for the self-diffusion of microspheres in concentrated solutions.

Computer simulations of diffusion in free solution

To compare measured MSD plots with theory, Monte Carlo simulations were carried out as described in Materials and Methods. As the trajectory length of the random walk was increased, $\rho(t)$ became more linear, similar to results computed for 2D diffusion (Qian et al., 1991) (Fig. 5 *A*). For each plot, $\rho_x(t)$, $\rho_y(t)$, and $\rho_z(t)$ were colinear for the first few time intervals, after which time they diverged (data not shown). These plots are predicted to be neither linear nor overlapping at larger t because a finite number of data points were collected.

The MSD plots for a simulated 3D random walk (Fig. 5 *A*) had the same qualitative shape as those determined experimentally for bead diffusion in free solution (Fig. 4, *B* and *C*). Variabilities of each point in the $\rho_x(t)$, $\rho_y(t)$, $\rho_z(t)$, and $\rho(t)$ plots for the simulated trajectory were in quantitative agreement with those measured for random bead diffusion (Fig. 5 *B*). These results support the conclusion that the particles in our samples diffused randomly in all three dimensions and that the measurement uncertainties introduced by the tracking algorithms were small compared with the intrinsic statistical variability in 3D particle trajectories.

SPT of small beads in living cells

Two applications of 3D tracking in living cells were demonstrated: bead diffusion in cytoplasm, and measurement of cell volume changes by the motion of beads at the cell surface. Small fluorescent latex beads (93 nm diameter) were microinjected into the cytoplasm of Swiss 3T3 fibroblasts and their 3D trajectories were measured. After microinjection, the beads were confined to small pockets of the cell, within which the beads diffused rapidly. These pockets de-

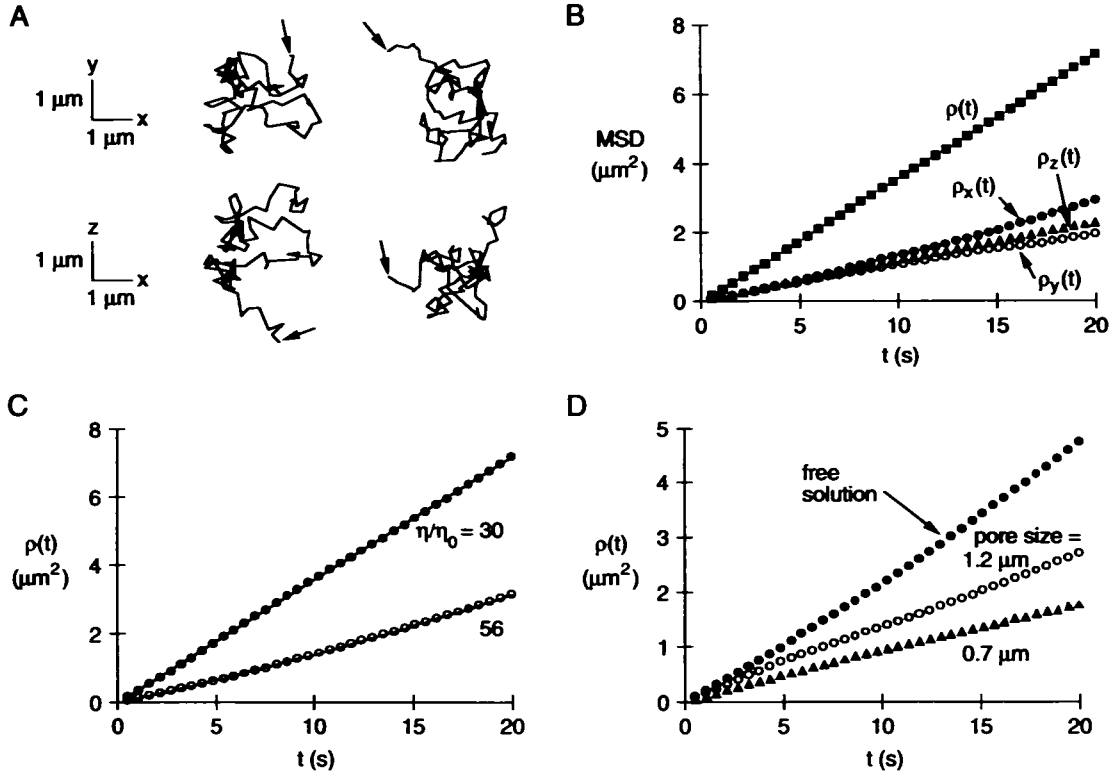

FIGURE 4 Three-dimensional SPT of beads in water-glycerol solutions and porous glass filters. The 3D position of a 264 nm red fluorescent particle was measured every 0.54 s for 15 min. (*A*) 100 steps of two 3D trajectories of a freely diffusing particle in an 83% aqueous glycerol solution having viscosity 60 cP at 27.5°C. Projections of trajectories onto the *x*-*y* and *x*-*z* plane are shown. Arrows indicate the initial bead positions. (*B*) Representative MSD plots for a freely diffusing particle in a 77% aqueous glycerol solution of viscosity 30. (*C*) Representative $\rho(t)$ curves for a freely diffusing particle in 77 and 83% aqueous glycerol solutions having viscosities 30 and 56 cP, respectively. (*D*) Representative $\rho(t)$ plots for a freely diffusing particle in free solution and in porous glass filters with 1.2 and 0.7 μm pore sizes.

creased slowly in size after microinjection; after 2–3 h, most beads appeared to be immobile. This rapid and confined motion is demonstrated by a representative MSD plot shown in Fig. 6 *A* (*filled circles*). The downward curvature of $\rho(t)$ indicates particle diffusion either within a confined volume or in an obstacle-filled environment (Saxton, 1987, 1989). The shape of this curve was qualitatively similar to that for a random walk confined within a cube with side length 0.25 μm (curve *b*). Quantitative values for bead diffusion coefficients in cell cytoplasm cannot be deduced from this data because the sampling rate of our instrument was not fast enough to measure the initial slope of the MSD plot.

Changes in cell volume were monitored from the *z* position of a small bead immobilized on the external surface of the cell plasma membrane. Three types of cells were compared: CHIP28-expressing CHO cells obtained by transient transfection with cDNA encoding CHIP28 water channels, nonexpressing cells that did not incorporate the cDNA, and nontransfected (control) cells that were never exposed to the CHIP28 cDNA. In the absence of osmotic driving forces (perfusion with 300 mOsm solution), bead *z* position was constant (Fig. 6 *B*). In response to a 150 mOsm perfusing solution, cell volume (and bead *z* position) increased because of osmotic water influx; cell volume (and bead *z* position) decreased when solution osmolality was returned to 300 mOsm. Osmotic water permeability in CHIP28-expressing cells was remarkably higher than in the nonexpressing and nontransfected cells as shown by the rate of *z* position change in response to an osmotic gradient. In four sets of experiments, the rate was increased by an average of 3.2-fold.

DISCUSSION

This study demonstrated three-dimensional tracking of single fluorescent particles using a weak cylindrical lens introduced into the detection path of an epifluorescence microscope. The resulting images contained a focus-dependent asymmetry that encoded particle *x*, *y*, and *z* coordinates. The transverse (*x*, *y*) coordinates were taken as the centroid of the image, and the axial (*z*) coordinate was computed in real-time from the degree and orientation of the image. Two algorithms were developed to analyze particle *z* position in real time. The first algorithm determined the projection width, and the second applied one-dimensional peak detection. *z* position was determined from algorithm parameters using calibration curves for an immobilized reference bead established at the beginning of an experiment. A focus-drive motor kept the in-focus plane close enough to the fluorescent particle so that the *z*-axis determination was accurate and unambiguous. The *x*, *y* coordinates of a particle were

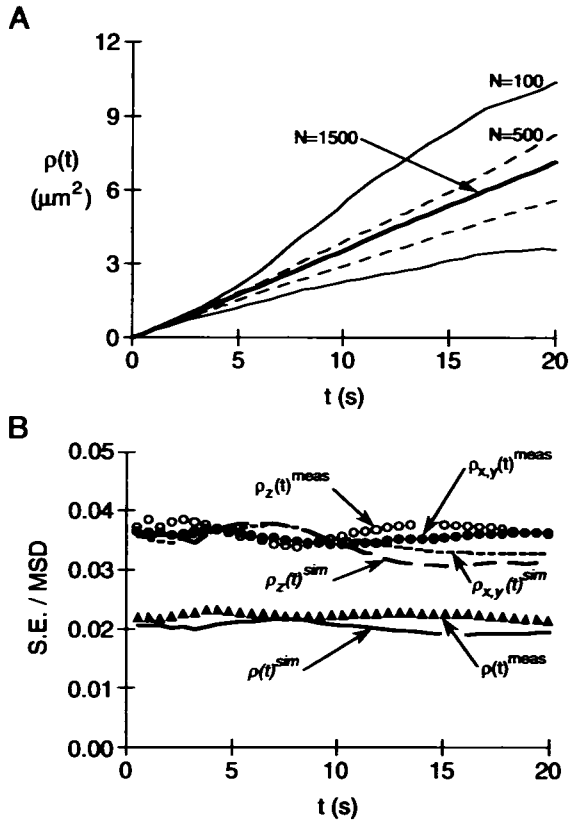

FIGURE 5 Computer simulations of MSD plots for 3D particle diffusion. (*A*) $\rho(t)$ for computer-simulated random walks of 100, 500, and 1500 steps in length. Step size was adjusted to give the same diffusion coefficient as that for a 264 nm bead freely diffusing in a 77% aqueous glycerol (viscosity 30 cP). (*B*) The ratio of the SE to mean value for $\rho_x(t)$, $\rho_y(t)$, $\rho_z(t)$ and $\rho(t)$. SE was calculated for the set of squared distances used to determine the mean. Curves are shown for a computer-simulated random walk and a measured 3D trajectory of a freely diffusing 264-nm bead having 1500 steps in length.

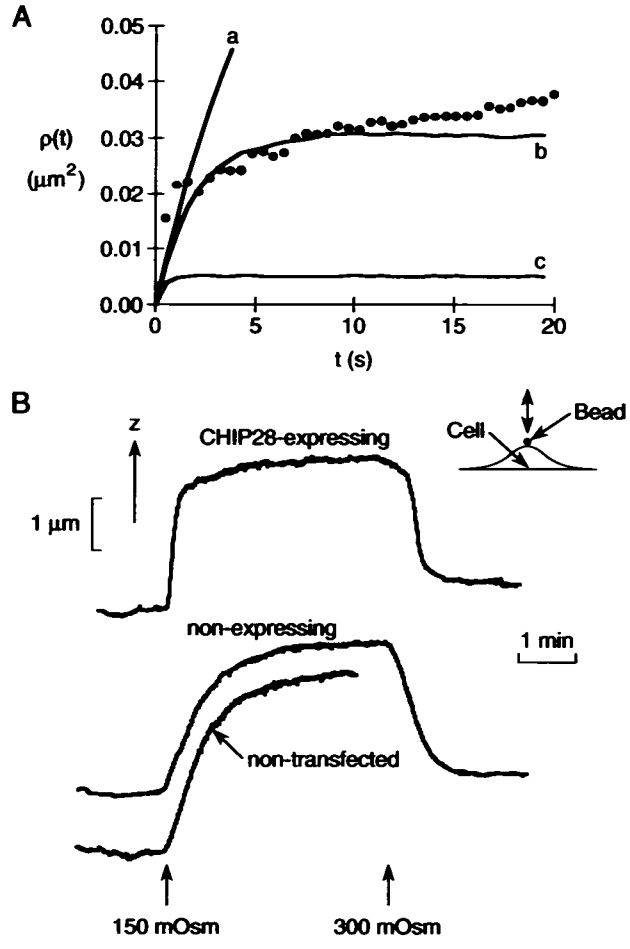

FIGURE 6 Applications of 3D SPT in living cells. (*A*) MSD plot for a bead microinjected into the cytoplasm of a Swiss 3T3 fibroblast (●). Solid lines are MSD plots for a computer-simulated random walk confined within a cube with side a) 0.50 μm, b) 0.25 μm, and c) 0.10 μm. Both simulated and measured trajectories were 1166 steps in length. (*B*) Measurement of osmotic water permeability in nontransfected and transfected CHO cells. The z position of a fluorescent bead immobilized at the cell surface was measured in response to perfusion with buffer of indicated osmolalities.

generally measured to within 5 nm, and the z coordinate was measured to within 12 nm.

A distinct advantage of the astigmatic aberration produced by the cylindrical lens is the alignment of the focus-dependent asymmetry with the rows and columns of the detector array. Every microscope objective contains some degree of focus-dependent spherical aberration that could potentially be used to deduce z position. However, these aberrations are dependent upon the microscope objective, and quantification of any asymmetries may require complex image recognition algorithms. With the cylindrical lens, the aberration is independent of the objective and, because of the alignment of the asymmetry with the detector array, quantification of the asymmetry is simple and rapid. The potential disadvantage of introducing astigmatic aberration is the degradation of the transverse (x, y) microscope resolution. This is apparent from a size comparison of the in-focus images with and without the cylindrical lens (Fig. 1). With the cylindrical lens, the full-width half-maximum of the image is ≈0.3 μm, whereas without the lens, it becomes ≈0.5 μm. If the particle images remain well separated, the main effect of the image degradation is to decrease the overall brightness of the image.

To measure z position accurately, the calibration curves established for an immobile particle must remain valid as the particle moves within a sample. From the theoretical analysis of Gibson and Lanni (1991), particle images produced out-of-focus are independent of the particle z position when the refractive index of the immersion oil matches that of the sample. The independence of $\Phi(z)$ on particle z position was confirmed by direct measurement in Fig. 3 *B*. For our experiments on diffusion of beads in model systems, the refractive indices were closely matched; the z measurements were accurate as demonstrated by the colinearity of $\rho_x(t)$, $\rho_y(t)$, $\rho_z(t)$ in the random diffusion measurements (Fig. 4 *B*). The analysis of Gibson and Lanni may be extended to a general requirement that the refractive index of the immersion medium in contact with an objective lens must equal that

of the sample. However, the refractive index of the immersion medium should be close to its recommended value to minimize degradations in image contrast and resolution (Gibson and Lanni, 1991). Hence, for experiments involving biological samples, a water immersion objective lens would be best because the refractive index of these samples is close to that of water. Air and oil objectives could be used if appropriate correction factors are included in the calibration curves.

The precision to which the x, y, z position of a particle could be resolved was limited by the signal-to-noise ratio of the image. Factors that reduced the signal-to-noise ratio included instrument microvibration, detector dark counts and read noise, low image intensities, and image smearing because of the nonzero exposure time. These factors also apply in two-dimensional tracking studies. The typical resolution for x, y position determination here was 5 nm, which was greater than that of 1–2 nm in a previous report of two-dimensional SPT (Gelles et al., 1988). This difference in x, y resolution was caused by differences in signal-to-noise ratios and effective pixel size. It should be noted that the overall spatial resolution of our instrument was limited by the accuracy of z position determination to $\approx$12 nm at 600 nm wavelength. Further improvement in spatial resolution may be obtained by increasing the effective pixel size and/or signal intensity.

The maximum sampling rate for 3D tracking was determined by the acquisition and analysis of a particle image. The exposure and data transfer time for a 12 bit 40 $\times$ 40 pixel image was approximately 150 ms. The algorithms described in this study were implemented on a 25 MHz 486DX computer and required computation time of approximately 150 ms, giving a 3–4 Hz maximum sampling rate. To measure faster particle motions, the sampling rate could be increased by several approaches. Computation time could be reduced by using a faster computer. Images could be stored for post-experiment processing as reported in previous two-dimensional SPT studies (De Brebander et al., 1989); however, a major disadvantage of image post-processing is that adjustment of the z position of the microscope stage cannot be accomplished during the experiment. Another approach would be to decrease the exposure time for image collection. However, in biological applications where particle fluorescence is low, brief exposure times may yield greater errors in position measurement.

Hysteresis and gear lash in the microscope fine focus control did not permit accurate determination of z position from the angular position of the motor. Because of this variability, many data points were required to generate calibration curves with high precision. This uncertainty associated with the mechanical movement of the stage also precluded high accuracy 3D SPT by continuous autofocusing control algorithms. Unlike an autofocusing method, our technique is capable of simultaneously tracking several particles by analysis of particle images.

The ability to track particles in three dimensions was demonstrated in artificial and biological systems. In artificial systems, the diffusion coefficient of particles in solutions of viscosities 30 and 56 cP solutions were in agreement with values predicted from the Stokes-Einstein equation. Bead diffusion decreased in the presence of an immobile network, as theoretically predicted. 3D SPT was also applied to measure the diffusion of beads within cells. Analysis of the trajectory of these particles indicated confined diffusion. The ability to track shape changes in cells was demonstrated by the measurement of water permeability in individual adherent cells in culture. The strategy of tracking fluorescent beads at the cell surface could also be applied to study volume regulatory phenomena in individual cells, and to correlate volume regulation with intracellular ion activities. The 3D SPT method introduced here also has potential applications to a number of other biological problems including: a) the directed, diffusive, and restricted motion of intracellular organelles, such as endocytic and secretory vesicles, providing information on the role of skeletal proteins and vesicular fusion in transport phenomena; b) the existence of immobile intracellular barriers to diffusive motions, such as the putative nuclear scaffold structure; and c) the direction of specific membrane components during cell motility and mitosis.

We thank Dr. Olivier Seksek for microinjection of fluorescent beads into cells, Dr. Tonghui Ma for preparing CHO cells transfected with CHIP28 water channels, and Drs. James R. Abney and Bethe Scalettar for helpful discussions.

This work was submitted in partial fulfillment of requirements for a Ph.D. thesis in Bioengineering (H. P. Kao) and was supported by National Institutes of Health grants DK43840 and DK35214.

REFERENCES

Couch, L. W. 1987. Digital and Analog Communication Systems. Macmillan, New York. 430–431.

De Brebander, M., H. Geerts, R. Nuydens, and R. Nuyens. 1989. Detection of gold probes with video-enhanced contrast microscopy: nanovid microscopy. *Am. J. Anat.* 185:282–295.

Geerts, H., M. De Brebander, R. Nuydens, S. Geuens, M. Moeremans, J. De May, and P. Hollenbeck. 1987. Nanovid tracking: a new automatic method for the study of mobility in living cells based on colloidal gold and video microscopy. *Biophys. J.* 52:775–782.

Gelles, J., B. J. Schnapp, M. P. Sheetz. 1988. Tracking kinesin-driven movements with nanometer-scale precision. *Nature.* 331:450–453.

Gibson, S. F., and F. Lanni. 1991. Experimental test of an analytical model of aberration in an oil-immersion objective lens used in three dimensional light microscopy. *J. Opt. Soc. Am. A.* 8:1601–1613.

Gonzalez, R. C., and P. Wintz. 1987. Digital Image Processing, 2nd ed. Addison-Wesley, Reading, MA. 334–340.

Gross, D. J., and W. W. Webb. 1988. Cell surface clustering and mobility of the liganded LDL receptor measured by digital video fluorescence microscopy. *In* Spectroscopic Membrane Probes. Vol. II. L. M. Loew, editor. CRC Press, Boca Raton, FL. 19–47.

Hiraoka, Y., J. W. Sedat, and D. A. Agard. 1990. Determination of the three-dimensional imaging properties of a light microscope system: partial confocal behavior in epifluorescence microscopy. *Biophys. J.* 57: 325–333.

Inoué, S. 1986. Video Microscopy. Plenum, New York. 334–338.

James, M. L., G. M. Smith, J. C. Wolford. 1985. Applied Numerical Methods for Digital Computation, 3rd ed. Harper & Row, New York. 396–397.

Lee, G., A. Ishihara, and K. A. Jacobson. 1991. Direct observation of brownian motion of lipids in a membrane. *Proc. Natl. Acad. Sci. USA.* 88: 6274–6278.

Ma, T., A. Frigeri, S.-H. Tsai, J. M. Verbavatz, and A. S. Verkman. 1993. Localization, and functional analysis of CHIP28k water channels in stably transfected chinese hamster ovary cells. *J. Biol. Chem.* 268:22756–22764.

Miner, C. S., and N. N. Dalton. 1953. Glycerol. Reinhold Publishing Corp., New York. 279–322.

Pusey, P. N., and R. J. A. Tough. 1985. Particle interactions. *In* Dynamic Light Scattering: Applications of Photon Correlation Spectroscopy. R. Pecora, editor. Plenum Press, New York. 85–179.

Qian, H., M. P. Sheetz, and E. L. Elson. 1991. Single particle tracking: analysis of diffusion and flow in two-dimensional systems. *Biophys. J.* 60:910–921.

Salmeen, I., P. Zacmanidis, G. Jesion, and L. A. Feldkamp. 1985. Motion of mitochondria in cultured cells quantified by analysis of digitized images. *Biophys. J.* 48:681–686.

Saxton, M. J. 1987. Lateral diffusion in an archipelago: the effect of mobile obstacles. *Biophys. J.* 52:989–997.

Saxton, M. J. 1989. Lateral diffusion in an archipelago: distance dependence of the diffusion coefficient. *Biophys. J.* 56:615–622.

Sheetz, M. P., S. Turney, H. Qian, and E. L. Elson. 1989. Nanometre-level analysis demonstrates that lipid flow does not drive membrane glycoprotein movements. *Nature.* 340:284–288.

Zen, K., J. Biwersi, N. Periasamy, and A. S. Verkman. 1992. Second messengers regulate endosomal acidification in Swiss 3T3 fibroblasts. *J. Cell Biol.* 119:99–110.

Zhang, F., G. M. Lee, and K. Jacobson. 1993. Protein lateral mobility as a reflection of membrane microstructure. *Bioessays.* 15:579–588.